Competing Effects of Local Solvation Structures on Chemical Shift Changes of Liquid Electrolyte

Qi You,[†] Yan Sun,[†,‡] Feng Wang,[¶] Jun Cheng,[*,†,¶,§] and Fujie Tang[*,‖,¶,§]

[†]*State Key Laboratory of Physical Chemistry of Solid Surface, iChEM, College of Chemistry and Chemical Engineering, Xiamen University, Xiamen, 361005, China*

[‡]*State Key Laboratory of Catalysis, iChEM, Dalian Institute of Chemical Physics, Chinese Academy of Sciences, Dalian, 116023, China.*

[¶]*Laboratory of AI for Electrochemistry (AI4EC), Tan Kah Kee Innovation Laboratory (IKKEM), Xiamen, 361005, China*

[§]*Institute of Artificial Intelligence, Xiamen University, Xiamen, 361005, China*

[‖]*Pen-Tung Sah Institute of Micro-Nano Science and Technology, Xiamen University, Xiamen, 361005, China*

E-mail: chengjun@xmu.edu.cn; tangfujie@xmu.edu.cn

Abstract

Understanding the solvation structure of electrolytes is critical for optimizing the electrochemical performance of rechargeable batteries, as it directly influences properties such as ionic conductivity, viscosity, and electrochemical stability. The highly complex structures and strong interactions in high-concentration electrolytes make accurate modeling and interpretation of their "structure-property" relationships even more challenging with spectroscopic methods. In this study, we present a machine learning-based approach to predict dynamic ^7Li NMR chemical shifts in LiFSI/DME electrolyte solutions. Additionally, we provide a comprehensive structural analysis to

interpret the observed chemical shift behavior in our experiments, particularly the abrupt changes in [7]Li chemical shifts at high concentrations. Using advanced modeling techniques, we quantitatively establish the relationship between molecular structure and NMR spectra, offering critical insights into solvation structure assignments. Our findings reveal the coexistence of two competing local solvation structures that shift in dominance as electrolyte concentration approaches the concentrated limit, leading to anomalous reverse of ^{7}Li NMR chemical shift in our experiment. This work provides a detailed molecular-level understanding of the intricate solvation structures probed by NMR spectroscopy, leading the way for enhanced electrolyte design.

Introduction

Electrolytes facilitate the transfer of ions between the anode and cathode, and their solvation structure can influence various electrochemical properties, such as conductivity,[1,2] viscosity,[3] and battery performance, including the electrochemical stable potential window (ESPW),[3,4] coulombic efficiency (CE),[5] and cycling reversibility.[6,7] The relative strength of interactions between the cation–solvent and cation-anion can give rise to different types of solvation structures in the electrolytes.[8–14] These structures significantly affect the formation of electrode-electrolyte interface,[6,15–18] the desolvation and diffusion process,[19,20] and reaction mechanism.[3,21,22] In recent years, highly concentrated electrolytes (HCEs) and localized highly concentrated electrolytes (LHCEs) are widely employed in electrochemical energy storage systems,[9,23] where the intricate solvation structures and strong interactions between solutes and solvents play a pivotal role in achieving high energy storage densities.[8,24,25] These factors make the accurate modeling and interpretation of their "structure-property" relationships particularly challenging. Consequently, revealing the solvation structures of electrolytes is the central topic in understanding these processes of interest.[26–28]

In the experiments, there have been several characterization methods used to illustrate solvation structures, including vibrational and nuclear magnetic resonance (NMR) spectro-

scopies. Specifically, Raman spectroscopy has often been employed to reveal the intensity of cation-anion associations.[8,9,13,29–34] NMR spectroscopy, a non-destructive and atom-specific technique, is particularly well-suited for investigating the molecular details of the chemical environments of the particular nucleus within solvation structures, since its signal is sensitive to the local chemical environment.[32,35–41] Apart from that, the experimental NMR spectroscopy reveals much more information about correlation times,[41,42] relaxation times[43,44] and exchange dynamics of the chemical components.[45] Nevertheless, how to connect the observed spectral changes to their intrinsic molecular structural changes is a very challenging task. For instance, experimental NMR spectroscopy has observed chemical shift variations with changing concentration, particularly in the context of ion coordination in glyme electrolytes.[1,37,46] While its solvation structural changes are hard to connect to the observed chemical shift. Some calculations, which employ density functional theory (DFT) calculation can provide some limited information into these trends for electrolytes, often employing cluster extraction with some complicated sampling methods.[35,36,39,40,47] There have been many static calculations attempting to explain the structure-spectrum relationship, using the Amsterdam Density Functional (ADF) package[35–39,48] or Gaussian package[40,47] to calculate ^{1}H, ^{25}Mg, ^{43}Ca, ^{67}Zn, ^{17}O, ^{7}Li NMR spectrum. However, experimental chemical shifts reflect a weighted average from various local sites, combining local structural and dynamic information. This averaging complicates signal resolution and makes it more challenging to evaluate the structure-spectrum relation.[43,47,49]

Molecular dynamics (MD) simulations allow for tracking the dynamic structural changes in various types of electrolytes, with classical force field models,[13,47,50] first-principles methods[14,51,52] and machine learning potentials.[53,54] However, the direct connections between the molecular structures to the experimental spectral observables are still challenging, due to the heavy computational cost of obtaining a single spectral response from the obtained MD configuration. Moreover, the delicate choices of configurational sampling when utilizing the NMR DFT calculation are too complicated to be implemented in the complex electrolyte sys-

tem.[47] Nevertheless, there are some attempts, by training on structural descriptors of solid state structures and their corresponding NMR chemical shifts, machine learning models can enhance the speed of chemical shift predictions while maintaining high accuracy.[49,55–58] Therefore, a robust computational method is essential, as a clear consensus on the relationship between the dynamic structural characteristics of electrolytes and their experimental spectral observables has not yet been established. Furthermore, validating the simulated structures and linking them to experimental observables remains a challenging task, one that could serve as a benchmark for the simulation.

In this paper, we propose a novel approach to connect the microscopic molecular structures and the spectroscopic features of the electrolyte. First, we combine two machine learning (ML) models for calculating dynamic NMR shifts: one MLP model for accelerating configuration sampling and another Neural Network (NN) model for rapid chemical shift prediction. To elaborate, we use the MLP model to generate a range of concentration trajectories. Subsequently, we conduct extensive sampling of electrolytes through prolonged MLMD simulations, creating chemical shift datasets from infrequent configurations within these simulations using the DFT method. The NN model is then trained and validated with this DFT-generated data, where the input features are the structural descriptor, such as Local Many-body Tensor Representation (LMBTR),[59,60] and the outputs are the chemical shifts. Finally, we use the NN-NMR model to calculate the dynamic ^{7}Li NMR spectra for various concentrations of LiFSI in DME solutions. We successfully reproduced the experimental observed anomalous reverse of ^{7}Li NMR chemical shift in our experiment when electrolyte concentration approaches the concentrated limit. Furthermore, by introducing one local structural parameter, called local structural index (LSI),[61–63] we quantitatively establish the structure-spectrum relationship, which helps clarify the solvation structure assignments. To this end, We find two different types of local solvation structures competing with each other, as electrolyte concentration approaches the concentrated limit, leading to anomalous reverse of ^{7}Li NMR chemical shift in our experiment. As such, we established a comprehensive

4

molecular-level understanding of the delicate microscopic molecular structures observed by using NMR spectroscopy. With our approach, one can track the complicated solvated structures changes in the electrolytes with different conditions, enabling precise control over the stability and solubility properties of electrolytes.

Method

Theoretical NMR Calculation

The methodology is illustrated in Fig. 1. For the structural exploration section, Machine Learning Molecular Dynamics (MLMD) simulations are conducted under the NVT ensemble with various initial structures of different concentrations pre-equilibrated from classical MD simulations. The Nose-Hoover thermostat is employed for generating the NVT ensembles. The temperature is set to 300 K and each simulation lasts 10 nanoseconds (ns) with a 0.5 fs time step. More details about the pre-equilibrium and the MLMD simulations are given in Sect. I of the Supporting Information (SI). For the construction of the NN model, we sparsely sample configurations from MLMD trajectories. Then we extract the first solvation shells around the Li^+ ions as clusters and label them, resulting in a DFT dataset containing about 28,000 ^7Li chemical shifts. All DFT calculations for NMR are performed by using Gaussian 16.[64] NMR calculations for clusters are conducted at the revTPSS[65,66]/pcSseg-1[67] level using the polarizable continuum model (PCM) solvation model.[68]

The principle of cluster extraction is to capture the first solvation shell around the given Li^+ ion while maintaining the integrity of surrounding molecules. The first solvation shell is identified by the first minimum position ~ 3.0Å after the main peak in the radial distribution function (RDF) between Li and O shown in Fig. S3(c). We consequently extract complete molecules that have atoms located within this region. However, in some cases, other nearby Li^+ ions occupy the space within the first coordination shell, as shown in the RDF of Li^+-Li^+ at 4M in Fig. S3(d), which exhibits a gentle peak around ~ 3.0Å. Thus, we grasp the entire

group of central atoms bonded to each other as one long-chain cluster. Although the cutoff distance between Li^+ ions is sufficiently set within the range of the first shell, we extend the distance to ~ 6.3Å to ensure the accurate local environment, which corresponds to the prominent peak position of RDF between Li^+ ions at 1-3 M.
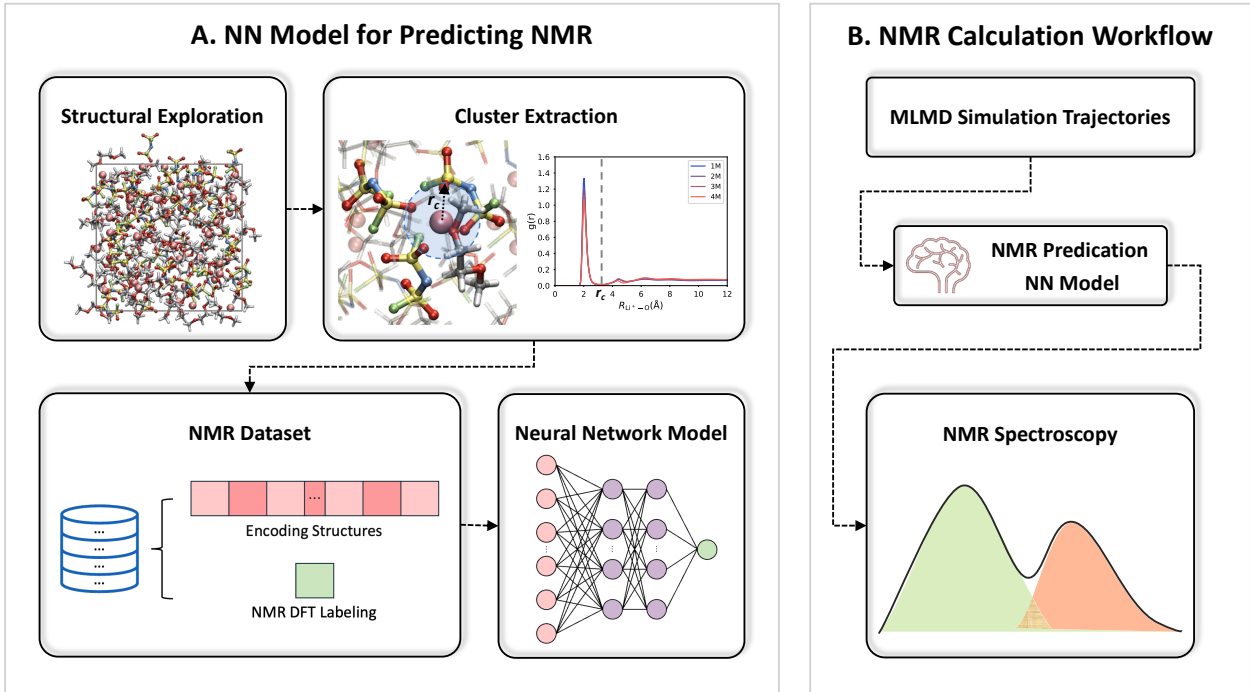

Figure 1: Workflow for predicting NMR spectroscopy. (Left) Technique approach to training a neural network (NN) model. Explore various structures for different concentrations, and extract clusters surrounding lithium ions. Subsequently, encode structures using the descriptor and calculate their corresponding chemical shifts. (Right) NMR prediction workflow. Generate trajectories using MLMD simulations, then utilize the obtained NMR prediction NN model to obtain NMR spectroscopy.

For the construction of the NMR dataset, we use the LMBTR descriptor to encode the structure. The LMBTR vectors for the Li^+ local environments are generated using the Dscribe package,[60] with a cutoff distance r_{cut} of 6 Å, parameters of k2 and k3 are listed in Tab. S2 in SI. The NN prediction model is initialized and trained in PyTorch, utilizing a hidden layer with three sequential layers, each containing 256 nodes. The learning rate is initialized at 10^3 and decayed inversely with each epoch at a decay rate of 32. The model undergoes validation using a 9/1 split for the training and testing sets, and an early stopping

mechanism is employed to prevent overfitting. We validate our NN-based NMR model using LiFSI/DME solutions. As shown in Fig. S5, the root-mean-square-error (RMSE) for the ^{7}Li isotropic values in the test set is ~ 0.13 ppm. Details of the NN model are provided in Sect. V of SI. It's worth mentioning that the NN model demonstrates outstanding efficiency, capable of rapidly predicting ^{7}Li shifts for large datasets, which would be much more time-consuming and costly with traditional DFT methods. The prior limitation to the model's prediction speed lies in the time required to convert molecular structures into descriptor vectors, which scales with the number of configurations and the dimension of vectors.

After obtaining the NN models, we predict the NMR spectra based on MD simulation trajectories. As shown in Fig. 1(b), we generate four 10 ns MLMD trajectories for 1, 2, 3 and 4 M, respectively. We grasp the snapshots in regular intervals to ensure the number of Li$^+$ ions is approximately 90,000 for every concentration, which is enough to sample the chemical spaces. These snapshots are then encoded by the LMBTR descriptor as inputs for the NN model to predict NMR chemical shifts, which are aggregated into histograms of NMR chemical shifts corresponding to the respective concentrations. The Full Width at Half Maximum (FWHM) obtained from Lorentzian fitting for experimental data are 0.008, 0.017, 0.020 and 0.019 for 1 M, 2 M, 3 M and 4 M, respectively. We use these values to fit the associated histograms into NMR spectra, ensuring that the mean values of the histograms and the peak position of NMR spectra align (Fig. 2(b)). The Lorentz function involved is: $Y(\omega) = A\frac{\gamma}{(\omega-\omega_0)^2+\gamma^2}$, where γ is the FWHM, ω_0 is the peak position, and A is a scaling factor.

Experimental NMR Measurement

Lithium bis(fluorosulfonyl)imide (LiFSI) and 1,2-dimethoxyethane (DME) are obtained from Duoduo Chemical Reagent Co., Ltd., with both chemicals having a purity of 99.99%. All sample preparation procedures for four electrolytes with different salt concentrations (1, 2, 3, and 4 M LiFSI) are conducted within an argon-filled glovebox to maintain anhydrous

conditions. [7]Li Nuclear Magnetic Resonance (NMR) spectroscopy is employed to characterize LiFSI/DME electrolytes of varying concentrations. Measurements were performed using a Bruker Avance III HD 400 MHz NMR spectrometer at room temperature. We conduct two repeated NMR measurements for every single concentration. The experimental NMR chemical shifts data are shown in Fig. 2(a).

Results and Discussion

NMR Spectra of LiFSI/DME Electrolytes with Different Concentrations

It is generally believed that in the dilute limit case, the solvated Li^+/FSI^- ions are fully separated by the solution DME molecules in the LiFSI/DME electrolytes, called solvent-separated ions pairs (SSIP) situation. As the concentration of LiFSI increases, the coordination numbers of the oxygen atoms of DME molecules around the Li^+ ions change. More complicated solvation structures, like contact ion pairs (CIPs), and ion aggregates (AGGs) are emerged.[3] This, in turn, affects the electron localization function (ELF) of the Li^+ ions,[50,69,70] resulting in altered shielding effects around the Li^+ ions and changes in the observed NMR chemical shifts. This mechanism underlies the variations seen in the experimental NMR spectra for LiFSI/DME at different concentrations, shown in the Fig. 2(a), our measurement is consistent with the previous reports.[32,37] As one can see, in the low concentration (1-3 M), the NMR chemical shift tends to shift upfield with the increasing LiFSI concentration. However, at 4 M LiFSI concentration, which is close to the saturated limit ($\sim$5.3 M) of LiFSI/DME solution, the peak is downfield shifted to -4.134 ppm, when compared with the results obtained on the 3 M case of -4.172 ppm. The sudden changes of the chemical shift obviously reflect the changes of the Li^+ ion solvation structures at various LiFSI concentrations.

To reveal the microscopic structural picture concerning the changes of the NMR chemical shift, we calculate the dynamic NMR spectra with the help of NN models, the data is pre-
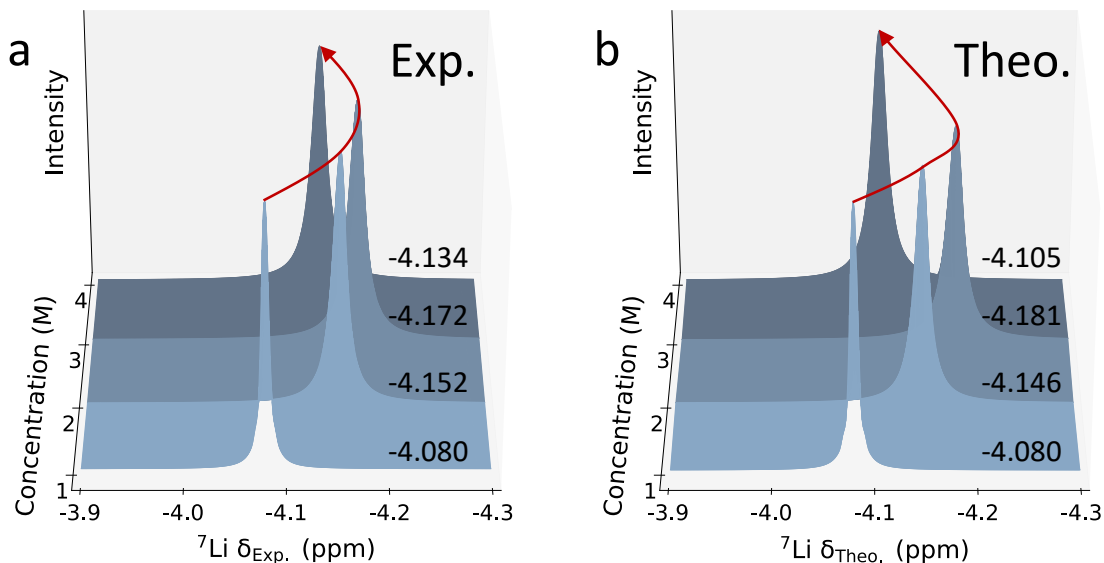
Figure 2: Comparison between computational and experimental results. (a) NMR experimental spectra of 1-4 M LiFSI/DME solutions. (b) Predicted NMR spectra of 1-4 M LiFSI/DME solutions. The calculated average chemical shift of the lowest concentration electrolytes has been aligned with the experimental value. The 95% confidence interval values for experimental and theoretical NMR chemical shift are ~ 0.006 ppm and ~ 0.002 ppm, respectively. The red curves are provided as visual guides.

sented in Fig. 2(b). Similarly to the experimental data, the theoretical NMR chemical shift is shifted upfield at low concentration, whereas it shifts downfield at 4 M. Notably, our theoretical NMR spectra are in excellent agreement with the experimental data, as we clearly show the NMR chemical shift changing point at 3 M concentration. The similar turning points observed in both experimental and theoretical NMR spectra suggest structural changes in the electrolytes as the LiFSI/DME solution approaches its saturation limit. Notably, at this concentration limit, the number of FSI^- ions becomes comparable to that of the solvent molecules (DME), resembling a scenario referred to as 'water-in-salts' (WiSs).[51,71] In this high-concentration regime, Li^+ ions are presumed to coordinate more frequently with FSI^- ions than with DME molecules, in contrast to the low-concentration case. Since Li^+ ions tend to bond with oxygen atoms in either FSI^- ions or DME molecules, the differing interaction strengths of the Li–O bonds with FSI^- or DME disrupt the delicate balance of electron

9

density around the Li$^+$ ions. This, in turn, affects the dynamic shielding effects and the NMR chemical shift. Nonetheless, the accurate reproduction of chemical shift variations in NMR due to changes in LiFSI concentration demonstrates the reliability of our NN models as effective tools for interpreting ^{7}Li NMR experiments involving electrolytes.

The Local Structures of the LiFSI/DME Electrolytes

The changes observed in the NMR spectra are a direct consequence of the evolving solvation structures. At the heart of this transformation lies the intricate interplay between cation-solvent and cation-anion interactions, which gives rise to distinct categories of the combinations of the cations, solvents and anions, such as SSIPs, CIPs, and AGGs, see Fig. 3(a). Before interpreting the complicated chemical shift variations due to the changes in LiFSI concentration, we first focus on the classifications of the solvation structures, based on the number of anions coordinated with Li$^+$, as shown in Fig. 3(b), which demonstrates that the high-number FSI$^-$ category (more than two) dominates as the concentration increases. Not surprisingly, in the low concentration case (1 M), the solvated Li$^+$/FSI$^-$ ions are separated by the solution DME molecules in the LiFSI/DME electrolytes, therefore, the coordination number of FSI$^-$ anions to Li$^+$ ion $n_{\text{FSI-}}$ is 0 or 1, which are corresponding to SSIP and CIP scenario. When the LiFSI concentration increases (2 or 3 M), the ratios of the SSIPs ($n_{\text{FSI-}} = 0$) and CIPs ($n_{\text{FSI-}} = 1$) decrease, the Li$^+$ ions are more bonded with FSI$^-$ anions leading to the increase of the AGGs ($n_{\text{FSI-}} = 2$ or 3). As more LiFSI salt is dissolved in the DME solution (4 M), approaching the saturation limit ($\sim$5.3 M),[37] the situation changes dramatically. The ratio of SSIPs and CIPs no longer continue to decrease but instead shows a slight increase compared to the 3 M case. Meanwhile, the proportion of lower-order AGGs ($n_{\text{FSI-}} = 2$ or 3, noted as AGGs) surprisingly decreases, while the proportion of higher-order AGGs ($n_{\text{FSI-}} > 3$, noted as AGGs+) continues to increase.

The terminology of SSIPs, CIPs, and AGGs can provide a framework for quantifying the solvation structures surrounding Li$^+$ ions. Meanwhile, the degree of inhomogeneity in the
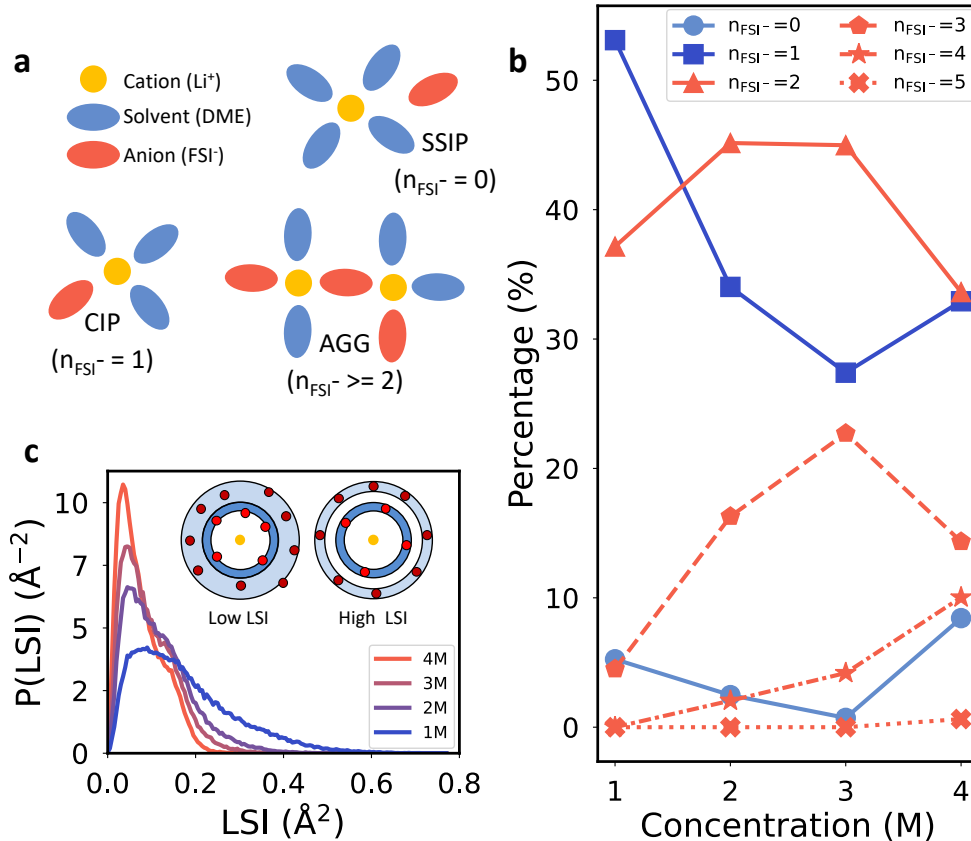
10

Figure 3: (a) Schematic diagram of solvation structure. (b) Solvation structure categories for 1-4 M LiFSI/DME solutions. n_{FSI^-} means the number of FSI anions coordinate to the Li$^+$. (c) Probability density distributions of local structural index (LSI) for 1-4 M LiFSI/DME solutions. (Insert) Schematic description of high-density-like and locally disordered (*left*) *vs.* low-density-like and locally ordered (*right*) environments, which correspond to *low* and *high* values of the LSI order parameter, respectively.

local molecular environment of Li$^+$ ions plays a crucial role in determining electron density around Li$^+$ nucleus, which in turn influences dynamic shielding effects and the resulting NMR chemical shift. Here, we utilized an order parameter, which associates local structure index (LSI)[61–63] to the individual Li$^+$ ions and its local neighbor oxygen pairs. In short, the LSI order parameter is the mean-squared-deviation among the radial distances corresponding to the set of the oxygen atoms that surround a given Li$^+$ ion, the LSI value is assigned as the inhomogeneity in the distribution of radial distances. The details of the definition can be referred to Sect. VI in SI. The schematic diagram provided in the insert of Fig. 3(c), which illustrates the different local atomic environments that can be distinguished and quantified

by the LSI order parameter. For instance, a Li^+ ion with a high LSI value is typically found in a more ordered local environment, where neighboring oxygen atoms are densely concentrated around $\sim$2.0 Å and sparsely distributed around $\sim$3.0 Å. This results in a clearer separation between the first and second coordination shells and a relatively low local atomic number density (as depicted on the right of the inset). Consequently, the electron density around the central Li^+ ion is less perturbed by the surrounding oxygen atoms, potentially leading to lower (absolute) NMR chemical shift values. Conversely, a Li^+ ion with a low LSI value resides in a locally disordered environment. This is characterized by a relatively high packing of neighboring oxygen atoms in the interstitial region and an elevated local atomic number density (as illustrated on the left of the inset). In such a densely packed and disordered atomic environment, the delicate balance of the surrounding electron density is disrupted, resulting in a higher NMR chemical shift value.

Now, Let us focus on the impact of LiFSI concentration changes on the LSI distribution, as shown in Fig. 3(c). At low concentrations, the LSI distribution exhibits a broad profile, suggesting a relatively ordered packing of neighboring oxygen atoms in the interstitial region. As the concentration of LiFSI increases in the DME solution, the interstitial region around the central Li^+ ion becomes more compressed. Consequently, the LSI distribution sharpens and displays a more pronounced peak. Consequently, the LSI distribution sharpens and displays a more pronounced peak. Simultaneously, a shoulder emerges at LSI $=\sim 0.15 Å^2$, indicating a concentration of neighboring oxygen atoms around $\sim 2.0 Å^2$, which forms a distinct sub-interstitial structure. As there are much more oxygen atoms aggregating around Li^+ ions, the sub-interstitial occurs between the first and the second coordination shell, which can be corroborated by the forward shift of the second coordination shell at 4 M, as shown in Fig. S3(c). This structure can also be analyzed using the RDFs between the Li^+ ions, see Fig. S3(d) of the SI. Notably, in the 4 M case, an additional peak appears around 3 Å in the Li^+-Li^+ RDF, indicating a direct interaction between two Li^+ ions. This suggests that the solvation structures of neighboring Li^+ ions are merging. Consequently, locally high-density

AGGs+-like structures, also referred to as micelle-like structures,[13,72] begin to emerge, as illustrated schematically in Fig. S6 of the SI. Under these conditions, the remaining Li^+ ions have a higher probability of forming ion pairs, such as SSIPs and CIPs. As shown in Fig. 3(b), the ratio of SSIPs and CIPs no longer decreases but instead exhibits a slight increase compared to the 3 M case.

Connections between Local Structures and NMR Chemical Shift

Our investigation focuses on elucidating the relationship between local structure and chemical shifts, emphasizing the need to unravel the complexities of the local environment and its corresponding isotropic characteristics. In the above analysis, we have interpreted the local chemical environment of Li^+ ions using chemical intuition, highlighting how the surrounding electron density is modulated by variations in the local environment. However, establishing a direct quantitative correlation between the semi-empirical relationship of the local chemical environment and the experimental NMR chemical shifts remains a more challenging task. To address this, we employ dimensionality reduction techniques, such as unsupervised principal component analysis (PCA). Specifically, we encode the local environment of the Li^+ ion using the LMBTR,[59] a structural descriptor that captures the local structure and its corresponding spectral information in a high-dimensional physical latent space. We then apply PCA to reduce the dimensionality of this representation, as illustrated in Fig. 4(a).

Notably, through structural-chemical shift analysis, we categorize the data points based on their distinct NMR values. The representative species corresponding to different NMR values exhibit strong correlations with their local chemical environments. Specifically, points with the lowest NMR values (red) are typically associated with SSIPs ($n_{FSI-} = 0$), while those with intermediate NMR values (yellow) correspond to CIPs ($n_{FSI-} = 1$). The dominant chemical shift region (green) is linked to AGGs ($n_{FSI-} = 2$ or 3), and the highest NMR values are observed for AGGs+ ($n_{FSI-} \geq 3$). The detailed assignment can be found in the Sect. VII of the SI. This finding aligns with chemical intuition, as discussed in the previous section,
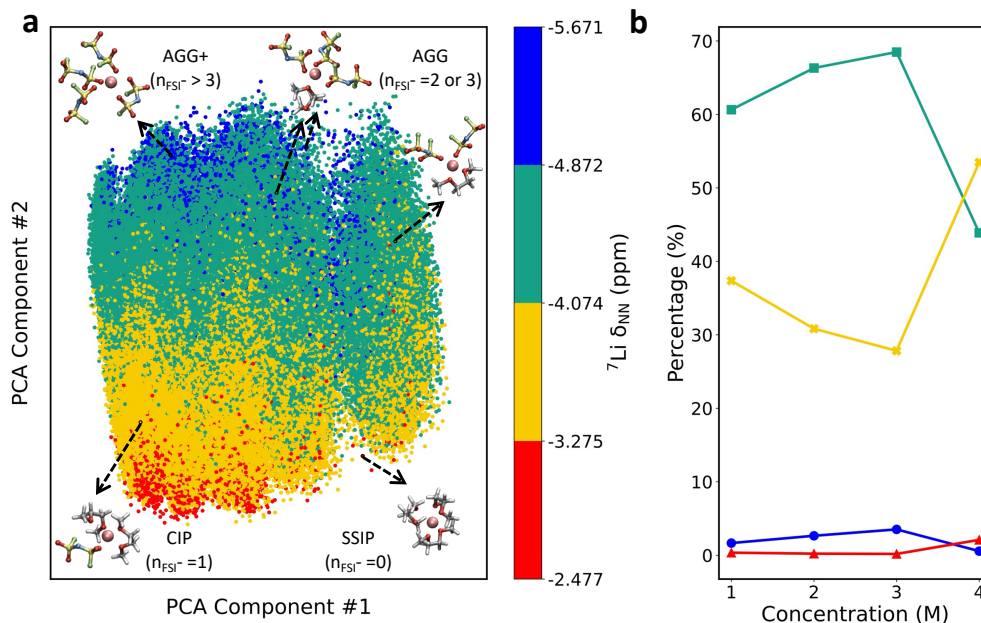
13

Figure 4: (a) Principal Component Analysis (PCA) of Li$^+$ solvation structural pattern mapping across various concentrations. Each point is associated with a NMR value from a local atomic motif, and the color code represents the corresponding NMR chemical shift value. The x- and y-axes represent the two most important principal components (PC#1 and PC#2). The representative spices of each color are chosen, as red for SSIP, yellow for CIP, AGGs for green and AGGs+ for blue. (b) The changes in the ratio of representative species for different colors with respect to varying LiFSI concentrations.

and underscores how the unsupervised PCA method effectively captures the influence of variations in the local environment on surrounding electron density.

Now, we can further investigate the changes in their populations to the varying LiFSI concentrations, as shown in Fig. 4(b). Notably, a dramatic shift occurs between 3 M and 4 M. Clearly, the most dominant structures are those with intermediate NMR values (yellow) and those with higher NMR values (green). The former shows a sudden increase, while the latter experiences a sharp decrease. Building on the insights from the discussion from the previous section, we infer that the increase in CIP structures (yellow) is due to the emergence of highly localized AGGs+ structures induced by Li$^+$-Li$^+$ interactions. Moreover, the detailed decomposition of the PCA analysis with respect to the different LiFSI concentrations, shown in Fig. S7 of the SI, reveals similar distributions across the various concentrations. It clearly

14

demonstrates the emergence of the CIP structures as the concentration increases from 3 M to 4 M.
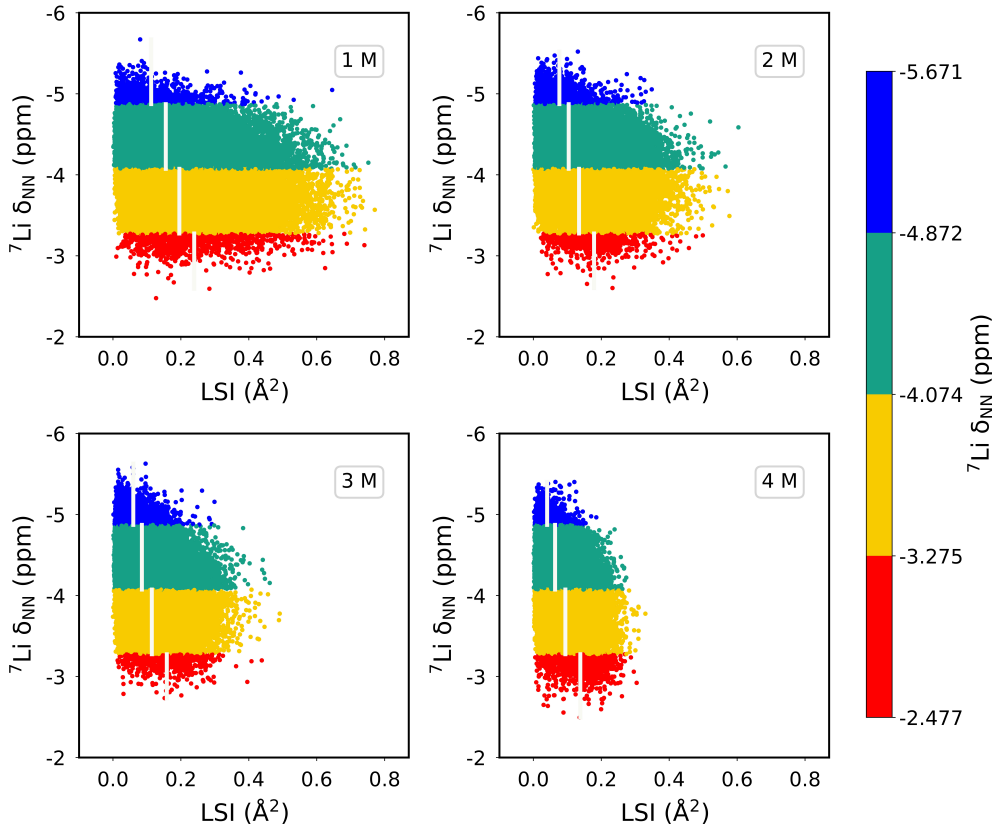

Figure 5: The correlation maps between the LSI and the chemical shift values for each concentration. The vertical lines represent the averaged LSI values of each region.

Going further, the results from the PCA are supported by the local structural parameters, such as the LSI. In Fig. 5, we present the NMR chemical shift values as a function of various LSI values. As the chemical shift values become higher, the LSI values simultaneously reduce, the tendency of which is consistent in four concentrations. According to the corresponding structures we assigned above, the average LSI value of blue region ($n_{FSI-} \geq 3$) at 4 M smaller than that at 3M, which means that the high hierarchy coordination number structures ($n_{FSI-} \geq 4$) replace this region instead of $n_{FSI-} = 3$. The reason for this phenomenon is that the high hierarchy coordination number configurations tend to have a filled sub-interstitial and form several long chain clusters of Li$^+$ and FSI$^-$ connected, the LSI of which are lower than those of clusters with $n_{FSI-} < 4$. Moreover, the clusters with $n_{FSI-} = 1$ (yellow region)

emerge along with the $n_{\text{FSI}^-} = 4$ case at 4 M, surrounding these AGGs+-like structures, ultimately leading to the lower LSI compared with 3 M case. This trend aligns with the findings from the local structure analysis in the previous section. Thus, the trend highlights the complex interplay between different local environments, with notable shifts driven by concentration effects. Moreover, the highly-localized AGGs+ structures induced by Li$^+$-Li$^+$ interactions can further reduce the diffusion constants of Li$^+$ ions, as they form additional ion pairs.[73] A similar scenario is observed in the diffusion behavior of hydronium and hydroxide in water,[74] the difference of the diffusion constant due to the presence of a hypercoordinate solvation structure. Nevertheless, the downfield shift of the ^{7}Li NMR chemical shift from 3 M to 4 M, is the signature of the emergence of the highly-localized AGGs structures and resulting less coordinated CIPs structures in the high concentration electrolyte.

Conclusion

To summarize, this study presents a novel machine learning-based approach for calculating dynamic NMR shifts in LiFSI/DME solutions by integrating an MLP model for configuration sampling and an NN model for chemical shift prediction. The NN-NMR model demonstrated both high accuracy and efficiency, with predictions closely matching experimental NMR spectra. As the concentration of LiFSI increases from 1 M to 3 M, changes in the solvation structure result in upfield shifts of the NMR chemical shifts, while at 4 M, the shifts move downfield. Through advanced modeling techniques, we build a quantitative relationship between molecular structure and NMR spectra, providing deep insights into solvation structure assignments. Our findings reveal the coexistence of two competing local solvation structures that exchange in dominance as electrolyte concentration approaches the upper limit, leading to observable changes in ^{7}Li NMR chemical shifts. This approach provides valuable insights into the relationship between solvation structure and NMR shifts, offering a more efficient and insightful method for studying electrolyte solutions. Overall,

this work enhances our understanding of electrolyte solvation and opens new pathways for optimizing electrolyte design based on molecular-level NMR insights.

Associated Content

Data Availability Statement

The code of automated workflow (ai2-kit) can be found at https://github.com/chenggroup/ai2-kit, and datasets for NN can be found at xxx upon acceptance of the manuscript.

Supporting Information

The Supporting Information is available free of charge at https://pubs.acs.org/xxx. Details on training errors of NN, AIMD setup, comparison between AIMD and MLMD, as well as NMR computational setup.

Notes

The authors declare no competing financial interest.

Acknowledgement

References

(1) Yoshida, K.; Nakamura, M.; Kazue, Y.; Tachikawa, N.; Tsuzuki, S.; Seki, S.; Dokko, K.; Watanabe, M. Oxidative-Stability Enhancement and Charge Transport Mechanism in Glyme–Lithium Salt Equimolar Complexes. J. Am. Chem. Soc. **2011**, _133_, 13121–13129.

(2) Chou, J.; Wang, Y.-H.; Wang, W.-P.; Xin, S.; Guo, Y.-G. Asymmetric electrode-electrolyte interfaces for high-performance rechargeable lithium-sulfur batteries. J. Electrochem. **2023**, _29_, 2217009.

(3) Xiao, P.; Yun, X.; Chen, Y.; Guo, X.; Gao, P.; Zhou, G.; Zheng, C. Insights into the solvation chemistry in liquid electrolytes for lithium-based rechargeable batteries. Chem. Soc. Rev. **2023**, _52_, 5255–5316.

(4) Peljo, P.; Girault, H. H. Electrochemical potential window of battery electrolytes: the HOMO–LUMO misconception. Energy Environ. Sci. **2018**, _11_, 2306–2309.

(5) Ko, S.; Obukata, T.; Shimada, T.; Takenaka, N.; Nakayama, M.; Yamada, A.; Yamada, Y. Electrode potential influences the reversibility of lithium-metal anodes. Nat. Energy **2022**, _7_, 1217–1224.

(6) Cheng, H.; Sun, Q.; Li, L.; Zou, Y.; Wang, Y.; Cai, T.; Zhao, F.; Liu, G.; Ma, Z.; Wahyudi, W.; Li, Q.; Ming, J. Emerging Era of Electrolyte Solvation Structure and Interfacial Model in Batteries. ACS Energy Lett. **2022**, _7_, 490–513.

(7) Sun, Q.; Du, H.-H.; Sun, T.-J.; Li, D.-T.; Cheng, M.; Liang, J.; Li, H.-X.; Tao, Z.-L. Sorbitol-Electrolyte-Additive Based Reversible Zinc Electrochemistry. J. Electrochem. **2024**, _30_, 2314002.

(8) Yamada, Y.; Yamada, A. Superconcentrated electrolytes for lithium batteries. J. Electrochem. Soc. **2015**, _162_, A2406.

(9) Jiang, L.-L.; Yan, C.; Yao, Y.-X.; Cai, W.; Huang, J.-Q.; Zhang, Q. Inhibiting Solvent Co-Intercalation in a Graphite Anode by a Localized High-Concentration Electrolyte in Fast-Charging Batteries. Angew. Chem. Int. Ed. **2021**, 60, 3402–3406.

(10) Ravikumar, B.; Mynam, M.; Rai, B. Effect of salt concentration on properties of lithium ion battery electrolytes: a molecular dynamics study. J. Phys. Chem. C **2018**, 122, 8173–8181.

(11) Callsen, M.; Sodeyama, K.; Futera, Z.; Tateyama, Y.; Hamada, I. The solvation structure of lithium ions in an ether based electrolyte solution from first-principles molecular dynamics. J. Phys. Chem. B **2017**, 121, 180–188.

(12) Zhang, Z.; Wang, J.; Qin, H.; Zhang, B.; Lin, H.; Zheng, W.; Wang, D.; Ji, X.; Ou, X. Constructing an Anion-Braking Separator to Regulate Local Li^+ Solvation Structure for Stabilizing Lithium Metal Batteries. ACS Nano **2024**, 18, 2250–2260.

(13) Efaw, C. M. et al. Localized high-concentration electrolytes get more localized through micelle-like structures. Nat. Mater. **2023**, 22, 1531–1539.

(14) Yao, N.; Chen, X.; Fu, Z.-H.; Zhang, Q. Applying Classical, Ab Initio, and Machine-Learning Molecular Dynamics Simulations to the Liquid Electrolyte for Rechargeable Batteries. Chem. Rev. **2022**, 122, 10970–11021.

(15) Gu, Y.; Hu, Y.-F.; Wang, W.-W.; You, E.-M.; Tang, S.; Su, J.-J.; Yi, J.; Yan, J.-W.; Tian, Z.-Q.; Mao, B.-W. An in-situ Raman Spectroscopic Study on the Interfacial Process of Carbonate-Based Electrolyte on Nanostructured Silver Electrode. J. Electrochem. **2023**, 29, 2301261.

(16) Liu, C.-X.; Zou, Z.-P.; Hu, M.-X.; Ding, Y.; Gu, Y.; Liu, S.; Nan, W.-J.; Ma, Y.-C.; Chen, Z.-B.; Zhan, D.-P.; Zhang, Q.-G.; Zhuang, L.; Yan, J.-W.; Mao, B.-W. The Determination of PZC and differential Capacitance Curve of Platinum-Alkaline Polymer Electrolyte Interfaces. J. Electrochem. **2024**, 30, 2303151.

(17) Chen, X.; Zhang, Q. Atomic Insights into the Fundamental Interactions in Lithium Battery Electrolytes. Acc. Chem. Res. **2020**, 53, 1992–2002.

(18) Zhang, X.-Q.; Tang, S.; Fu, Y.-Z. Recent advances of functional electrolyte additives for lithium-sulfur batteries. J. Electrochem. **2023**, 29, 2217005.

(19) Gupta, A.; Manthiram, A. Designing Advanced Lithium-Based Batteries for Low-Temperature Conditions. Adv. Energy Mater. **2020**, 10, 2001972.

(20) Hou, J.; Yang, M.; Wang, D.; Zhang, J. Fundamentals and Challenges of Lithium Ion Batteries at Temperatures between -40 and 60 °C. Adv. Energy Mater. **2020**, 10, 1904152.

(21) Zhang, G.; Peng, H.-J.; Zhao, C.-Z.; Chen, X.; Zhao, L.-D.; Li, P.; Huang, J.-Q.; Zhang, Q. The Radical Pathway Based on a Lithium-Metal-Compatible High-Dielectric Electrolyte for Lithium–Sulfur Batteries. Angew. Chem. Int. Ed. **2018**, 57, 16732–16736.

(22) Jia, H.-H.; Hu, C.-J.; Zhang, Y.-X.; Chen, L.-W. A Review on Solid-State Li-S Battery: From the Conversion Mechanism of Sulfur to Engineering Design. J. Electrochem. **2023**, 29, 2217008.

(23) Cao, X.; Jia, H.; Xu, W.; Zhang, J.-G. Localized high-concentration electrolytes for lithium batteries. J. Electrochem. Soc. **2021**, 168, 010522.

(24) Lukatskaya, M. R.; Feldblyum, J. I.; Mackanic, D. G.; Lissel, F.; Michels, D. L.; Cui, Y.; Bao, Z. Concentrated mixed cation acetate "water-in-salt" solutions as green and low-cost high voltage electrolytes for aqueous batteries. Energy Environ. Sci. **2018**, 11, 2876–2883.

(25) Chen, L. et al. A 63 m Superconcentrated Aqueous Electrolyte for High-Energy Li-Ion Batteries. ACS Energy Lett. **2020**, 5, 968–974.

(26) Ming, J.; Cao, Z.; Li, Q.; Wahyudi, W.; Wang, W.; Cavallo, L.; Park, K.-J.; Sun, Y.-K.; Alshareef, H. N. Molecular-Scale Interfacial Model for Predicting Electrode Performance in Rechargeable Batteries. ACS Energy Lett. **2019**, 4, 1584–1593.

(27) Gupta, A.; Bhargav, A.; Jones, J.-P.; Bugga, R. V.; Manthiram, A. Influence of Lithium Polysulfide Clustering on the Kinetics of Electrochemical Conversion in Lithium–Sulfur Batteries. Chem. Mater. **2020**, 32, 2070–2077.

(28) Chen, S.; Zheng, J.; Yu, L.; Ren, X.; Engelhard, M. H.; Niu, C.; Lee, H.; Xu, W.; Xiao, J.; Liu, J.; Zhang, J.-G. High-Efficiency Lithium Metal Batteries with Fire-Retardant Electrolytes. Joule **2018**, 2, 1548–1558.

(29) Wang, J.; Yamada, Y.; Sodeyama, K.; Chiang, C. H.; Tateyama, Y.; Yamada, A. Superconcentrated electrolytes for a high-voltage lithium-ion battery. Nat. Commun. **2016**, 7, 12032.

(30) Li, T.; Zhang, X.-Q.; Yao, N.; Yao, Y.-X.; Hou, L.-P.; Chen, X.; Zhou, M.-Y.; Huang, J.-Q.; Zhang, Q. Stable Anion-Derived Solid Electrolyte Interphase in Lithium Metal Batteries. Angew. Chem. Int. Ed. **2021**, 60, 22683–22687.

(31) Bi, S.; Salanne, M. Cluster analysis as a tool for quantifying structure–transport properties in simulations of superconcentrated electrolyte. Chem. Sci. **2024**, 15, 10908–10917.

(32) Jiang, K. S.; Hobold, G. M.; Guo, R.; Kim, K.-H.; Melemed, A. M.; Wang, D.; Zuin, L.; Gallant, B. M. Probing the Functionality of LiFSI Structural Derivatives as Additives for Li Metal Anodes. ACS Energy Lett. **2022**, 7, 3378–3385.

(33) Chaffin, V. O.; Pessanha, M. C.; Alves, W. A. Solvation structures formed in the $MgCl_2$:$AlCl_3$-dimethoxyethane system: A look through Raman and IR spectroscopies. Vib. Spectrosc. **2019**, 100, 167–171.

(34) Hahn, N. T.; Driscoll, D. M.; Yu, Z.; Sterbinsky, G. E.; Cheng, L.; Balasubramanian, M.; Zavadil, K. R. Influence of Ether Solvent and Anion Coordination on Electrochemical Behavior in Calcium Battery Electrolytes. ACS Appl. Energy Mater. **2020**, 3, 8437–8447.

(35) Deng, X.; Hu, M. Y.; Wei, X.; Wang, W.; Chen, Z.; Liu, J.; Hu, J. Z. Natural abundance ^{17}O nuclear magnetic resonance and computational modeling studies of lithium based liquid electrolytes. J. Power Sources **2015**, 285, 146–155.

(36) Hu, J. Z.; Rajput, N. N.; Wan, C.; Shao, Y.; Deng, X.; Jaegers, N. R.; Hu, M.; Chen, Y.; Shin, Y.; Monk, J.; Chen, Z.; Qin, Z.; Mueller, K. T.; Liu, J.; Persson, K. A. ^{25}Mg NMR and computational modeling studies of the solvation structures and molecular dynamics in magnesium based liquid electrolytes. Nano Energy **2018**, 46, 436–446.

(37) Wan, C.; Hu, M. Y.; Borodin, O.; Qian, J.; Qin, Z.; Zhang, J.-G.; Hu, J. Z. Natural abundance ^{17}O, ^6Li NMR and molecular modeling studies of the solvation structures of lithium bis(fluorosulfonyl)imide/1,2-dimethoxyethane liquid electrolytes. J. Power Sources **2016**, 307, 231–243.

(38) Hu, J. Z.; Jaegers, N. R.; Hahn, N. T.; Hu, W.; Han, K. S.; Chen, Y.; Sears, J. A.; Murugesan, V.; Zavadil, K. R.; Mueller, K. T. Understanding the solvation-dependent properties of cyclic ether multivalent electrolytes using high-field NMR and quantum chemistry. JACS Au **2022**, 2, 917–932.

(39) Chen, Y.; Jaegers, N. R.; Wang, H.; Han, K. S.; Hu, J. Z.; Mueller, K. T.; Murugesan, V. Role of solvent rearrangement on Mg^{2+} solvation structures in dimethoxyethane solutions using multimodal NMR analysis. J. Phys. Chem. Lett. **2020**, 11, 6443–6449.

(40) Im, J.; Halat, D. M.; Fang, C.; Hickson, D. T.; Wang, R.; Balsara, N. P.; Reimer, J. A. Understanding the Solvation Structure of Li-Ion Battery Electrolytes Using DFT-Based Computation and ^1H NMR Spectroscopy. J. Phys. Chem. B **2022**, 126, 9893–9900.

(41) Allen, J. P.; Szczuka, C.; Smith, H. E.; Jónsson, E.; Eichel, R.-A.; Granwehr, J.; Grey, C. P. Coordination of dissolved transition metals in pristine battery electrolyte solutions determined by NMR and EPR spectroscopy. Phys. Chem. Chem. Phys. **2024**, 26, 19505–19520.

(42) Hu, J. Z.; Jaegers, N. R.; Hu, M. Y.; Mueller, K. T. In situ and ex situ NMR for battery research. J. Phys. Condens. Matter **2018**, 30, 463001.

(43) Lin, M.; Liu, X.; Xiang, Y.; Wang, F.; Liu, Y.; Fu, R.; Cheng, J.; Yang, Y. Unravelling the fast alkali-ion dynamics in paramagnetic battery materials combined with NMR and deep-potential molecular dynamics simulation. Angew. Chem. Int. Ed. **2021**, 60, 12547–12553.

(44) Allen, J. P.; O'Keefe, C. A.; Grey, C. P. Quantifying Dissolved Transition Metals in Battery Electrolyte Solutions with NMR Paramagnetic Relaxation Enhancement. J. Phys. Chem. C **2023**, 127, 9509–9521.

(45) Zhou, L.; Leskes, M.; Liu, T.; Grey, C. P. Probing Dynamic Processes in Lithium-Ion Batteries by In Situ NMR Spectroscopy: Application to $Li_{1.08}Mn_{1.92}O_4$ Electrodes. Angew. Chem. Int. Ed. **2015**, 54, 14782–14786.

(46) Plewa-Marczewska, A.; Kalita, M.; Marczewski, M.; Siekierski, M. NMR studies of equilibriums in electrolytes: Ionic pairing in glymes. Electrochim. Acta **2010**, 55, 1389–1395.

(47) Atwi, R.; Chen, Y.; Han, K. S.; Mueller, K. T.; Murugesan, V.; Rajput, N. N. An automated framework for high-throughput predictions of NMR chemical shifts within liquid solutions. Nat. Comput. Sci. **2022**, 2, 112–122.

(48) Hu, W.; Jaegers, N. R.; Winkelman, A. D.; Murali, S.; Mueller, K. T.; Wang, Y.; Hu, J. Z. Modelling complex molecular interactions in catalytic materials for energy storage and conversion in nuclear magnetic resonance. Front. Catal. **2022**, 2, 935174.

(49) Lin, M.; Xiong, J.; Su, M.; Wang, F.; Liu, X.; Hou, Y.; Fu, R.; Yang, Y.; Cheng, J. A machine learning protocol for revealing ion transport mechanisms from dynamic NMR shifts in paramagnetic battery materials. Chem. Sci. **2022**, 13, 7863–7872.

(50) Yao, N.; Chen, X.; Sun, S.-Y.; Gao, Y.-C.; Yu, L.; Gao, Y.-B.; Li, W.-L.; Zhang, Q. Identifying the lithium bond and lithium ionic bond in electrolytes. Chem **2024**, 11, 102254.

(51) Goloviznina, K.; Serva, A.; Salanne, M. Formation of Polymer-like Nanochains with Short Lithium–Lithium Distances in a Water-in-Salt Electrolyte. J. Am. Chem. Soc. **2024**, 146, 8142–8148.

(52) Perez Beltran, S.; Cao, X.; Zhang, J.-G.; Balbuena, P. B. Localized High Concentration Electrolytes for High Voltage Lithium–Metal Batteries: Correlation between the Electrolyte Composition and Its Reductive/Oxidative Stability. Chem. Mater. **2020**, 32, 5973–5984.

(53) Wang, F.; Sun, Y.; Cheng, J. Switching of redox levels leads to high reductive stability in water-in-salt electrolytes. J. Am. Chem. Soc. **2023**, 145, 4056–4064.

(54) Wang, F.; Ma, Z.; Cheng, J. Accelerating Computation of Acidity Constants and Redox Potentials for Aqueous Organic Redox Flow Batteries by Machine Learning Potential-Based Molecular Dynamics. J. Am. Chem. Soc. **2024**, 146, 14566–14575.

(55) Paruzzo, F. M.; Hofstetter, A.; Musil, F.; De, S.; Ceriotti, M.; Emsley, L. Chemical shifts in molecular solids by machine learning. Nat. Commun. **2018**, 9, 4501.

(56) Cordova, M.; Engel, E. A.; Stefaniuk, A.; Paruzzo, F.; Hofstetter, A.; Ceriotti, M.; Emsley, L. A Machine Learning Model of Chemical Shifts for Chemically and Structurally Diverse Molecular Solids. J. Phys. Chem. C **2022**, 126, 16710–16720.

(57) Lin, M.; Fu, R.; Xiang, Y.; Yang, Y.; Cheng, J. Combining NMR and molecular dynamics simulations for revealing the alkali-ion transport in solid-state battery materials. Curr. Opin. Electrochem. **2022**, 35, 101048.

(58) Xu, F.; Guo, W.; Wang, F.; Yao, L.; Wang, H.; Tang, F.; Gao, Z.; Zhang, L.; E, W.; Tian, Z.-Q.; Cheng, J. Towards a Unified Benchmark and Framework for Deep Learning-Based Prediction of Nuclear Magnetic Resonance Chemical Shifts. 2024; `https://arxiv.org/abs/2408.15681`.

(59) Huo, H.; Rupp, M. Unified representation of molecules and crystals for machine learning. Mach. Learn.: Sci. Technol. **2022**, 3, 045017.

(60) Laakso, J.; Himanen, L.; Homm, H.; Morooka, E. V.; Jäger, M. O.; Todorović, M.; Rinke, P. Updates to the DScribe library: New descriptors and derivatives. J. Chem. Phys. **2023**, 158, 234802.

(61) Shiratani, E.; Sasai, M. Growth and collapse of structural patterns in the hydrogen bond network in liquid water. J. Chem. Phys. **1996**, 104, 7671–7680.

(62) Shiratani, E.; Sasai, M. Molecular scale precursor of the liquid–liquid phase transition of water. J. Chem. Phys. **1998**, 108, 3264–3276.

(63) Biswajit Santra, F. M., Robert A. DiStasio Jr.; Car, R. Local structure analysis in ab initio liquid water. Mol. Phys. **2015**, 113, 2829–2841.

(64) Frisch, M. J. et al. Gaussian˜16 Revision C.01. 2016; Gaussian Inc. Wallingford CT.

(65) Tao, J.; Perdew, J. P.; Staroverov, V. N.; Scuseria, G. E. Climbing the Density Functional Ladder: Nonempirical Meta–Generalized Gradient Approximation Designed for Molecules and Solids. Phys. Rev. Lett. **2003**, 91, 146401.

(66) Perdew, J. P.; Ruzsinszky, A.; Csonka, G. I.; Constantin, L. A.; Sun, J. Workhorse

Semilocal Density Functional for Condensed Matter Physics and Quantum Chemistry. Phys. Rev. Lett. **2009**, <u>103</u>, 026403.

(67) Jensen, F. Segmented Contracted Basis Sets Optimized for Nuclear Magnetic Shielding. <u>J. Chem. Theory Comput.</u> **2015**, <u>11</u>, 132–138.

(68) Miertuš, S.; Scrocco, E.; Tomasi, J. Electrostatic interaction of a solute with a continuum. A direct utilizaion of AB initio molecular potentials for the prevision of solvent effects. <u>Chem. Phys.</u> **1981**, <u>55</u>, 117–129.

(69) Savin, A.; Jepsen, O.; Flad, J.; Andersen, O. K.; Preuss, H.; von Schnering, H. G. Electron Localization in Solid-State Structures of the Elements: the Diamond Structure. <u>Angew. Chem. Int. Ed.</u> **1992**, <u>31</u>, 187–188.

(70) Krivdin, L. B. Recent advances in the liquid-phase ^{6,7}Li nuclear magnetic resonance. <u>Magn. Reson. Chem.</u> **2023**, <u>61</u>, 138–161.

(71) Zheng, J. et al. Understanding Thermodynamic and Kinetic Contributions in Expanding the Stability Window of Aqueous Electrolytes. <u>Chem</u> **2018**, <u>4</u>, 2872–2882.

(72) Verma, A.; Schulze, M. C.; Colclasure, A. Micelle-like bulk structure of localized high-concentration electrolytes. <u>Joule</u> **2024**, <u>8</u>, 10–12.

(73) Zhang, P.; Jin, H.; Wang, T.; Wang, M. Insight into the effect of lithium-dendrite suppression by lithium bis(fluorosulfony)imide/1,2-dimethoxyethane electrolytes. <u>Electrochim. Acta</u> **2018**, <u>277</u>, 116–126.

(74) Chen, M.; Zheng, L.; Santra, B.; Ko, H.-Y.; DiStasio Jr, R. A.; Klein, M. L.; Car, R.; Wu, X. Hydroxide diffuses slower than hydronium in water because its solvated structure inhibits correlated proton transfer. <u>Nat. Chem.</u> **2018**, <u>10</u>, 413–419.